

Synthetic Bone-Like Structures Through Omnidirectional Ceramic Bioprinting in Cell Suspensions

Sara Romanazzo, Thomas Gregory Molley, Stephanie Nemeč, Kang Lin, Rakib Sheikh, John Justin Gooding, Boyang Wan, Qing Li, Kristopher Alan Kilian,* and Iman Roohani*

The integration of hierarchical structure, chemistry, and functional activity within tissue-engineered scaffolds is of great importance in mimicking native bone tissue. Bone is a highly mineralized tissue which forms at ambient conditions by continuous crystallization of the mineral phase within an organic matrix in the presence of bone residing cells. Despite recent advances in the biofabrication of complex engineered tissues, replication of the heterogeneity of bone microenvironments has been a major challenge in constructing biomimetic bone scaffolds. Herein, inspired by the bone biomineralization process, the first example of bone mimicking constructs by 3D writing of a novel apatite-transforming ink in a supportive microgel matrix with living cells is demonstrated. Using this technique, complex bone-mimicked constructs are made at room temperature without requiring invasive chemicals, radiation, or postprocessing steps. This study demonstrates that mineralized constructs can be deposited within a high density of stem cells, directing the cellular organization, and promoting osteogenesis *in vitro*. These findings offer a new strategy for fabrication of bone mimicking constructs for bone tissue regeneration with scope to generate custom bone microenvironments for disease modeling, multicellular delivery, and *in vivo* bone repair.

mineralized matrix in a hierarchical structural organization.^[7] This has posed a significant challenge in developing a synthetic approach to replicate the heterogeneous environment of bone, which allows creating mechanically-stable mineralized constructs and at the same time enables embedding bone relevant cells and other temperature-chemical-radiation sensitive biomolecules. In this domain, a plethora of materials including bioceramics,^[8–12] cell-laden hydrogels,^[5,13,14] and synthetic thermoplastics,^[15] in conjunction with additive manufacturing techniques have been employed to create synthetic bone matrices.

The rapid advances in 3D printing techniques of bioceramics (such as lithographic printing) have facilitated the fabrication of complex bone-mimicked structures from a range of bioceramic materials.^[9] For example, Zhang et al. have recently developed Haversian bone-mimicked scaffolds from Akermanite using

digital laser processing technique.^[10] They designed a series of scaffolds with an integrated hierarchical structure including Haversian canals, Volkmann canals, and cancellous bone and showed their favorable osteogenesis and angiogenesis both *in vitro* and *in vivo*. Despite the robustness and precision of recent 3D printing techniques for bioceramics, prints should be ultimately sintered at high temperatures before proceeding to be seeded with cells or implantation *in vivo*. The sintering step is necessary for removing the organic components that are primarily mixed with the ceramic powder and also for solidifying the structure. In doing that, temperature-sensitive components


1. Introduction

Bone tissue is an essential part of the human body, playing roles in mechanical support and protection, mineral homeostasis, and hematopoiesis. Over the past years, there have been many efforts to mimic bone tissue in the form of 3D tissue-engineered constructs for the regeneration of the damaged tissue, disease modeling, drug screening, or simply studying cell–cell crosstalk in the bone microenvironment.^[1–6]

Structurally, bone tissue is an organic–inorganic composite where metabolically active cells are embedded within a highly

Dr. S. Romanazzo, K. Lin, R. Sheikh, Prof. K. A. Kilian, Dr. I. Roohani
School of Chemistry
Australian Centre for Nanomedicine
University of New South Wales
Sydney, NSW 2033, Australia
E-mail: k.kilian@unsw.edu.au; iman.roohani@unsw.edu.au
T. G. Molley, S. Nemeč, Prof. K. A. Kilian
School of Materials Science and Engineering
University of New South Wales
Sydney, NSW 2033, Australia

Prof. J. J. Gooding
School of Chemistry
Australian Centre for NanoMedicine and the ARC Centre of Excellence in
Convergent Bio-Nano Science and Technology
University of New South Wales
Sydney, NSW 2033, Australia
B. Wan, Prof. Q. Li
School of Aerospace, Mechanical and Mechatronic Engineering
University of Sydney
Sydney, NSW 2006, Australia

 The ORCID identification number(s) for the author(s) of this article can be found under <https://doi.org/10.1002/adfm.202008216>.

DOI: 10.1002/adfm.202008216

such as live cells or growth factors cannot be printed with scaffolds. This is a similar challenge when using thermoplastic materials for creating bone scaffolds.^[15] The other drawback of sintering is the formation of a solid microstructure, typically consisting of highly crystalline micrometer-sized grains,^[16] which do not replicate the micro and nanostructure of bone tissue. Some studies have strongly suggested that heat-treatment and formation of a solid microstructure in-turn reduce the bioactivity of the material in interaction with osteoprogenitor cells in vivo.^[17,18]

To address drawbacks associated with the heating, many efforts have been shifted toward developing techniques that operate under mild conditions.^[19,20] Lode et al. took advantage of the hydroxyapatite forming ability of calcium phosphate cements, which are commonly used as bone replacement materials and set under physiological condition, to develop an α -tricalcium phosphate-based paste.^[12] They showed that the paste can be extruded into a range of bioceramic-based scaffolds in vitro without requiring sintering. Despite the outstanding relevance of this approach, scaffolds cannot be printed with live cells. Once printed, they should be post-treated in humid environments followed by submerging in an aqueous solution for a long period.^[12–22] This is an essential step for solidifying the construct and removing the organic components before cell-seeding or subsequent treatments. The other downside of the techniques is that scaffolds must be printed by continuous stacking of 2D monolayers. This greatly limits the type of structures that can be generated, which often require supports to produce the complex features and overhangs, typical of biological structures.

One of the prominent alternatives to mimic the 3D nature of the cell-rich bone matrix under mild conditions is by using cell-laden polymeric hydrogels.^[14,23,24] However, they too fail to replicate the densely mineralized environment of the bone tissue. Some studies have addressed this by incorporation of inorganic particles or embedding osteoprogenitor cells to secrete mineral nodules after a long period of culture in vitro.^[25–27] In these instances, the mineral portion is typically randomly scattered and restricted to small volumetric percentages which do not replicate the densely packed mineralized bone tissue. In a pioneering work by Thrivikarman et al., they developed a biomimetic approach where they employed a supersaturated calcium and phosphate medium in combination with a noncollagenous protein analog to direct the deposition of nanoscale apatites on collagen embedded with osteoprogenitor cells.^[13] Although this

approach is the closest approximation to mimicking the bone nanoenvironment, it cannot generate rigid 3D constructs with micro–macro scale architecture similar to bone.

In this paper, we demonstrate the first example of freeform printing of bone-mimetic constructs at room temperature with living cells, without harsh chemicals or radiation and post-processing steps (Figure 1). Our technique utilizes a chemically stabilized gelatin microsphere support bath, where the optimized yield-stress properties support the omnidirectional printing of a bone mineral-transforming ink in the presence of live cells. This technique, labeled as ceramic omnidirectional bioprinting in cell-suspensions (COBICS), provides solutions to the major challenges in generation of bone mimicked tissue engineering constructs mimicking the bone microenvironment. COBICS is capable of printing complex and biologically relevant architecture constructs without the need for sacrificial support materials, on-spot and without laborious postprocessing steps which are two of the biggest challenges in additive manufacturing techniques for bone mimetic constructs. The ability to print nanostructured bone-mimetic ceramics within cell-laden biological materials in free-form with control over macro- and micro-architecture, provides scope for complex bone mimicry and real-time bone reconstruction in clinical settings.

2. Results and Discussion

2.1. A Fast-Setting Apatite Transforming Calcium Phosphate Ink

COBICS is enabled through freeform writing of a novel ceramic-based ink within a gelatin microsphere suspension, where yield-stress characteristics of the suspension support the printed ceramic structure and nanoprecipitation “locks” the structure in place (Figure 2A). The ceramic ink, which hereafter is referred to as “calcium phosphate ink (CaP-ink),” is a calcium phosphate-based formulation that quickly solidifies in aqueous environments while the integrity of extruded filaments is retained (Figure 2B, left). The CaP-ink takes advantage of the setting mechanism of premixed calcium phosphate cements in aqueous solutions.^[28] One of the classes of premixed calcium phosphate cements consist of a mixture α -tricalcium phosphate (α -TCP) powder as the main component and nonaqueous carriers. However, the main disadvantage of such premixed cements is eliciting toxicity when printing in presence of living cells. In the CaP-ink, α -TCP

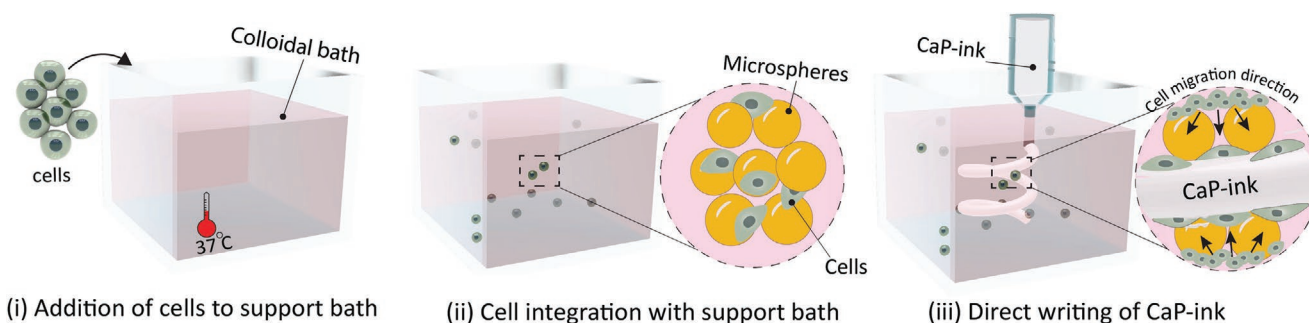


Figure 1. Overview of the process of omnidirectional printing of highly mineralized bone mimicked constructs under mild conditions and in the presence of live cells.

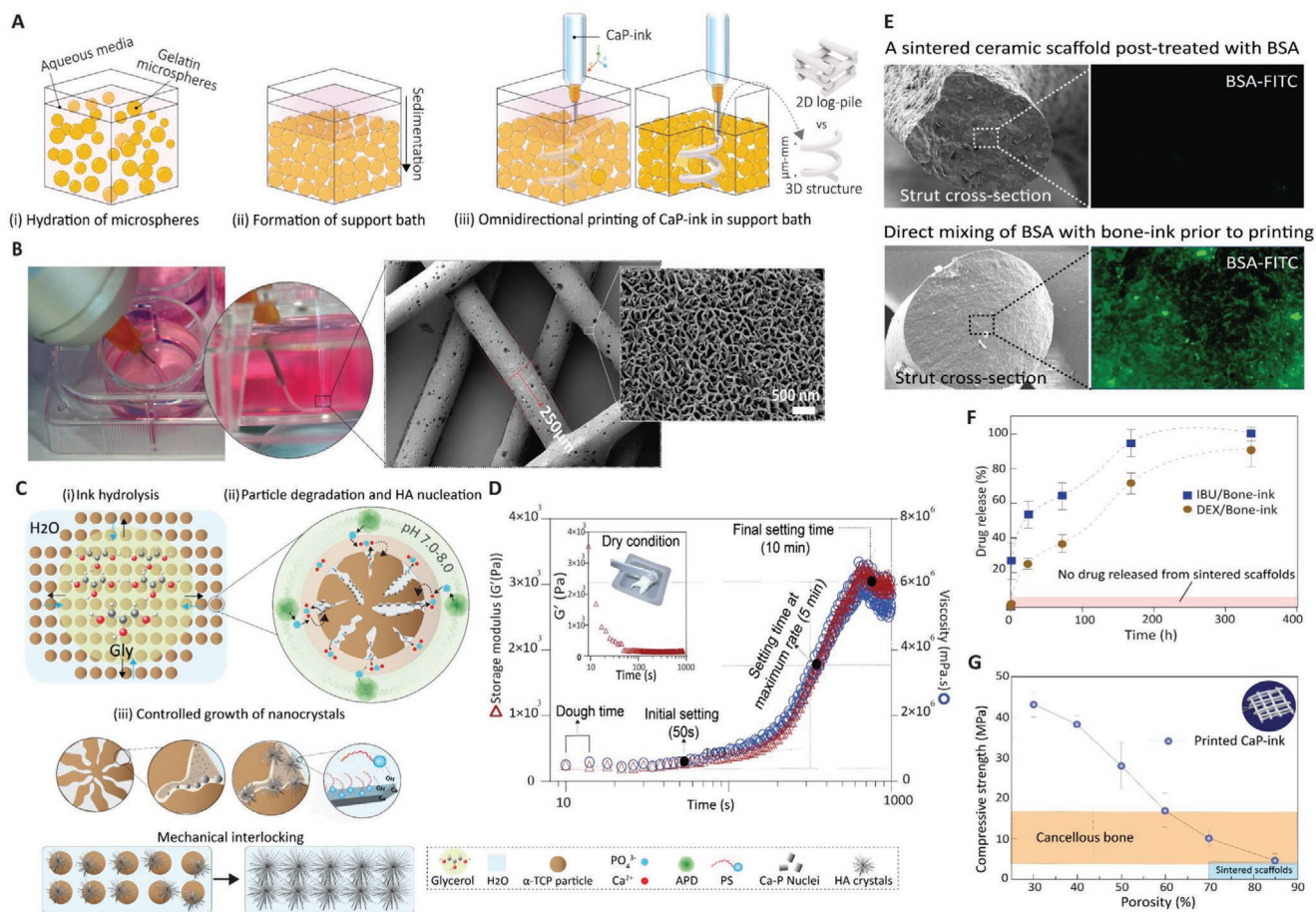


Figure 2. A) Free-form writing the CaP-ink in a suspension of gelatin microspheres with properties of a yield-stress fluid; 3D printing of complex structures versus structures generated by stacking of 2D monolayers. B) Representative image of direct extrusion of CaP-ink in culture media (Pore size: ≈ 500 and $1500 \mu\text{m}$ (X-Y plane) and $250 \mu\text{m}$ (Z plane), and 100% interconnectivity between the pores) and scanning electron micrographs demonstrating the nanostructured interface. C) The mechanism for CaP-ink nanoprecipitation and solidification: i) hydrolytic surface degradation of α -TCP as glycerol is replaced with water; ii) Ca-P nucleation and growth catalyzed by ammonium phosphate dibasic (APD); iii) polyoxyethylenesorbitan monooleate (PS) directs nanocrystal growth and crystal entanglement. D) Storage modulus (red triangles) and apparent viscosity (blue circles) of ink as a function of time in humid and dry (inset) condition. E) Distribution of bovine serum albumin labeled with fluorescein isothiocyanate (FITC) in cross-section of scaffolds incorporated by submerging a sintered scaffold in the protein solution (top) or direct mixing of the protein with ink (bottom). F) Comparative drug release profiles of dexamethasone (brown circles) and ibuprofen (blue squares) loaded into CaP-ink scaffolds and sintered hydroxyapatite scaffolds showing higher controlled release when drugs are incorporated in ink. G) Compressive strength of printed CaP-ink compared to cancellous bone (orange) and sintered scaffolds (light blue).

particles are homogeneously dispersed in glycerol, containing ammonium phosphate dibasic and the surfactant polyoxyethylenesorbitan monooleate. Glycerol acts as the carrier for α -TCP particles which facilitates extrusion of particles from printing nozzles.

Upon extrusion of the CaP-ink into aqueous environments, such as Milli-Q water, phosphate buffer saline and cell culture media, glycerol is replaced with water and hydrolysis of the α -TCP particles occurs at the interface (Figure 2C, i). During hydrolysis, ammonium phosphate increases the pH and concentration of PO₄³⁻ in the microenvironment, which facilitates nucleation and growth of calcium-deficient hydroxyapatite (HA) nanocrystals and ultimately quick setting of the CaP-ink (Figure 2C,ii). The pH change of the aqueous solution occurs during the initial setting time (within 5–10 min, depending on the concentration of ammonium phosphate)

as the result of exposure to the ink, then pH remains stable. Concerning altering the pH of cell culture medium, extrusion of ink did not change the color of cultures during the initial setting time and further during incubation with cells for 24 h, in comparison to control groups (without ink). The non-ionic surfactant mitigates the large crack formation by modulating the growth rate of nanocrystals and ensuring a uniform crystal growth. This modulation may occur by interaction of hydrated calcium ions located on the surface of HA crystals with the oxyethylene groups of a nonionic surfactant to form hydrogen bonds (CaOH \cdots O(CH₂CH₂)₂). We propose that this novel formulation of CaP-ink facilitates fast in situ solidification through nanocrystallization in aqueous environments, converting the inorganic ink to mechanically interlocked bone apatite nanocrystals (Figure 2C,iii; and Figure S1, Supporting Information).

For ease of preliminary analysis, we printed the CaP-ink directly in cell culture media (Figure 2B, left). Scanning electron microscopy analysis (SEM) revealed a porous microstructure consisting of an entangled network of uniformly sized nanocrystals that resembles bone's inorganic matrix (Figure 2B, right). The ink setting occurs upon immediate contact with aqueous media. The initial set occurred in less than 1 min, reaching its maximum rate after 5 min, with complete setting by 10 min postprinting. Despite a quick setting time, and hardening in humid conditions, the CaP-ink remained flowable when present in dry conditions and it showed a decreasing trend in storage modulus under rotational shear forces over time. In fact, under humid conditions, the complex viscosity and storage modulus of the ink increased by orders of magnitude compared to dry conditions (Figure 2D).

To identify the optimum weight fraction of CaP-ink components for ensuring a sound print, we mixed the ink components at a variety of ratios and assessed injectability, cohesion, setting time, and printability of the ink (Figure S2, Supporting Information). The glycerol had a significant effect on the injectability, printability, and cohesion. Increasing the glycerol improved the injectability, but adversely affected ink's cohesion. Excess glycerol (>35 wt%) resulted in merging the printed filaments (Figure S2A, Supporting Information), and a low amount of glycerol (<23 wt%) caused blockage of nozzles. Addition of ammonium phosphate substantially shortened the setting time from 30 to 3 min, but promoted formation of cracks in filaments after setting (Figure S2B–D, Supporting Information). We speculate that crack formation is a result of a rapid contraction of the filaments during setting or created hydrostatic pressure due to replacing glycerol with water. Increasing surfactant concentration attenuated the nonuniform crystal growth; however, at >5.0 wt% setting time was retarded (Figure 2D). We found that an optimal concentration of 65.8 wt% α -TCP, 26.1 wt% glycerol, 4.7 wt% polyoxyethylene-sorbitan monooleate, and 3.3 wt% ammonium phosphate, led to robust printing and setting time.

In contrast to current 3D printing techniques for bioceramics, COBICS enables the homogenous volumetric incorporation of bioactive molecules at high concentrations within the printed scaffold. A model protein, fluorescein isothiocyanate labeled bovine serum albumin (FITC-BSA), was incorporated in the ink prior to printing. Protein distribution was compared to the common approach of immersing sintered HA scaffolds in the protein solution. Fluorescence characterization indicates BSA had spread throughout the CaP-ink filament, in contrast to perimeter localization in sintered scaffolds (Figure 2E). Dexamethasone and ibuprofen, two commonly used drug models, were incorporated into the CaP-ink prior to printing. In contrast to immediate release of physiosorbed drug from sintered scaffolds, which resulted in no detection of drug after the first minute, the CaP-ink showed sustained drug release profiles with 60% by day 3 and 100% by day 15 (Figure 2F).

For FITC-BSA, ibuprofen, and dexamethasone, the total mass of the molecule in respect to the mass of the ink for each scaffold was 0.0005, 0.5, and 0.5 wt%, respectively. We also tested the drugs at supratherapeutic concentrations (5 and 10 wt%) and the setting time and ink integrity remained intact. The ink stability is mainly sensitive to excessive addition of

aqueous or organic phases within which biomolecules are dissolved since wet-phases alter the rheology attributes, integrity, and kinetics of crystallization in the ink. Therefore, we speculate that at concentrations which biomolecules are therapeutically effective (substantially lower than the mass of ink), size, charge, and chemistry of the biomolecules may not dictate a significant change in ink properties.

The compressive strength of printed scaffolds was measured at a range of porosities (30–85%) by changing the pore size, after keeping the scaffolds in phosphate-buffered saline (PBS) for 1 week at 37 °C. The compressive strength of the constructs was in the range of strength of cancellous bone and higher than that for sintered scaffolds (Figure 2G).

2.2. 3D Printing of Complex Bone-Mimetic Architectures in Yield-Stress Microgel Suspensions

To enable free-form printing of 3D shapes with the CaP-ink and cells, we set off to optimize a support bath consisting of a yield-stress support matrix to hold the construct in place. Microscale particle suspensions have been demonstrated to support printing of soft materials in complex structures due to the yield-stress properties,^[29–33] however, the efficacy of such suspensions in support of mineralized constructs has not been reported before. Therefore, toward an optimal yield-stress matrix capable of free-form bioceramic printing, we first performed computational studies to determine the interrelationship between CaP-ink filament diameter and microspheres size to obtain a sound print. By analyzing combinations of microspheres, spatial distribution, and various configurations of CaP-ink filaments, either horizontal, vertical, or with a 45° inclination (Figure 3A), it was found, that the peak deformation values raised with the increase in the size of gelatin microspheres (Figure 3B). In addition, the largest ink deformation was more likely to be concentrated in the bottom region of filaments, regardless of size of microspheres and geometry of printed CaP-ink filaments (Figure 3B–D). Moreover, thinner filaments led to larger magnitudes of deformation (Figure 3B,C). When comparing ink with similar diameter, the spiral geometry further increased peak deformation values compared to straight filaments (Figure 3C,D). Decreasing filament diameter resulted in less indented deformation, especially in the vertical and 45° inclination placements. When analyzing the deformation distribution for the linear filaments of the same diameter supported in different size microsphere suspensions, we found that the peak deformation values increased with microsphere size. With respect to the spatial orientation of the filaments, the deformation decreased when changing the orientation from vertical to horizontal (Figure 3B).

Based on our modeling results, we moved into the fabrication of microspheres smaller or equal to diameter of 400 μ m: the smallest group had a diameter of $14.0 \pm 6.31 \mu$ m (S), then a medium size of $93.3 \pm 45.8 \mu$ m (M) and the largest group of microspheres developed had $401 \pm 187 \mu$ m (L) (Figure 3E). Printing fidelity was then evaluated as a function of microsphere size (Figure 3F). Medium-sized gelatin microspheres (M) were synthesized using a standard water-in-oil emulsion

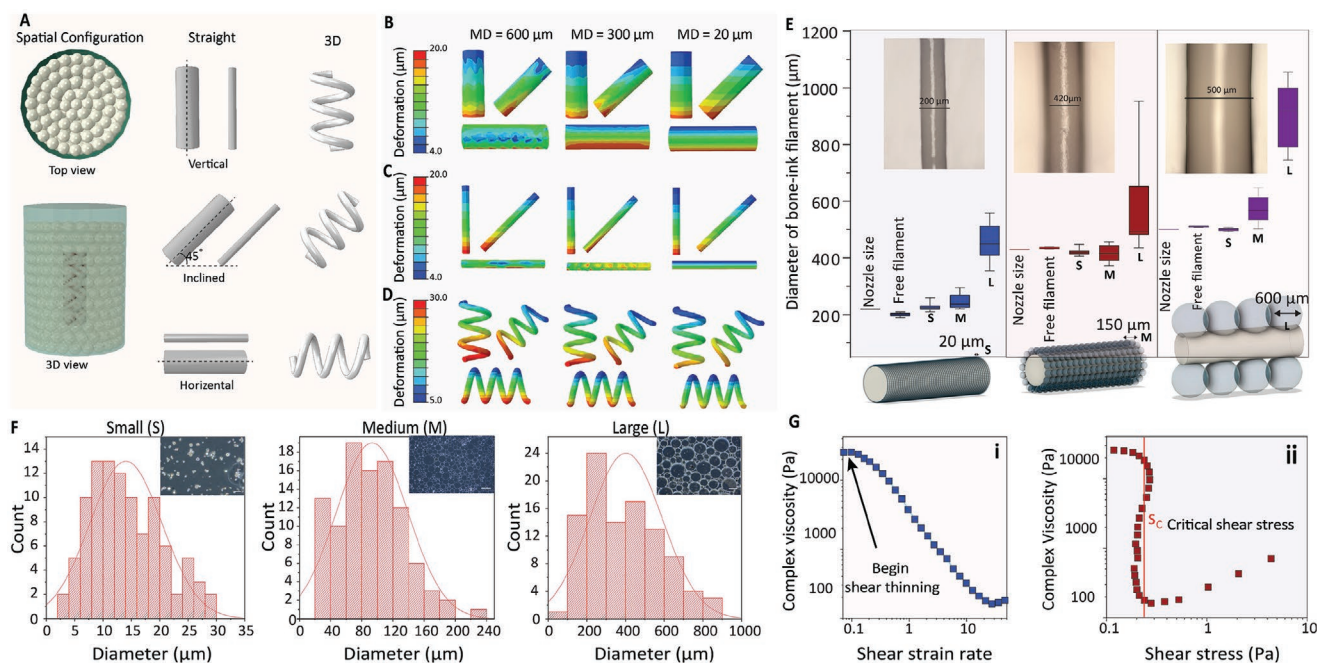


Figure 3. Computational modeling of the interaction between CaP-ink filaments and gelatin microspheres in the support bath to identify conditions for the minimum ink deformation after printing. A) Representative arrangements of ink filaments with a diameter of 600 and 200 μm in gelatin microspheres: straight (90°), inclined (45°), and horizontal (0°) in single-strand and spiral forms. Deformation maps of ink filaments in the single-strand form with a diameter of B) 600 μm , C) 200 μm , and D) in spiral-form with a diameter of 200 μm printed in a bath containing gelatin microspheres with a diameter of 600, 300, and 20 μm . MD = microsphere diameter. E) Experimental validation of gelatin microsphere size on the deformation of ink filaments extruded through nozzles with diameters of 220, 430, and 500 μm . F) Size distribution and optical image of crosslinked gelatin microspheres by glutaraldehyde at fully hydrated state: Optical image (20 \times) of hydrated microparticles synthesized with span surfactant and histogram of size distribution, scale bar 50 μm (S); Optical image (4 \times) of hydrated microparticles synthesized under standard conditions (M) with the histogram of size distribution; Optical image (4 \times) of hydrated microparticles synthesized under slow conditions (L) with the histogram of size distribution. Scale bars 350 μm . G) Rheology of glutaraldehyde treated gelatin microsphere bath: i) Complex viscosity versus shear strain rate and, ii) complex viscosity versus shear stress.

at 40 $^\circ\text{C}$ with rigorous rotation to form droplets, followed by cooling to 10 $^\circ\text{C}$ to physically crosslink the microspheres. We fabricated gelatin microspheres that would dissolve at 37 $^\circ\text{C}$ so that printed structures could be harvested directly. However, for some applications, a stable suspension may be advantageous, e.g., for using the gelatin as a complex microstructured extracellular matrix. To stabilize the suspension, we added glutaraldehyde to the freshly made microspheres with stirring. The simplicity of the system will allow other crosslinking schemes including mild approaches using enzymes,^[34] thereby tuning the susceptibility to degradation in biological environments. Shear rheology confirmed that our gelatin microsphere suspensions behave as yield-stress fluids—responding as a rigid body under low shear stress, while as a viscous fluid under high shear stress (Figure 3G).

Next, we explored free-form printing of the CaP-ink in the different suspensions of gelatin microspheres. First, microspheres were hydrated in cell culture media, allowing the formation of a homogeneous bath. Here, the microspheres pack together and enter a “jammed” state where they behave like a solid under equilibrium conditions but flow like a liquid under shear forces. In this way, high-fidelity deposition of ink occurs as the mobile printing needle locally fluidizes the suspension. Once the needle front progresses, the bath destabilizes and locks the printed ink in place.

Imaging the ink setting within the support bath demonstrated firm adhesion of the gelatin microspheres to the nanostructured CaP-ink interface (Figure 4A,B; and Movie S1, Supporting Information). Microspheres in direct contact with the CaP-ink remained fixed, while the surrounding microspheres retained yield-stress fluid characteristics (Movies S2–S4, Supporting Information). When the CaP-ink was deposited in the support bath, the extruded filaments did not disintegrate and kept their rigidity even at diameters as small as 200 μm (Figure 4A,left; and Movie S5, Supporting Information). This confirmed the ability to accurately print delicate structures, that by proximity nucleates nanocrystals which mimic natural bone structures. This was visualized by the increased surface roughness of the ink compared to initial contact (Figure 4A, right). Increasing the microsphere size resulted in deviations in extruded filament diameter compared to nozzle diameter with $L > M > S$ (Figure 3E).

Using COBICS, we printed mimics of the human osseous labyrinth (Figure 4D), trabecular bone (Figure 4E), and Haversian canals (Figure 4F). In these cases, we used computer 3D models to print bone-like structures in a suspension of gelatin microspheres, so that after fabrication the printed bone is recovered through gelatin dissolution at 37 $^\circ\text{C}$ (Figure S4, Supporting Information). The versatility of the emulsion approach will allow incorporation of virtually any matrix protein within

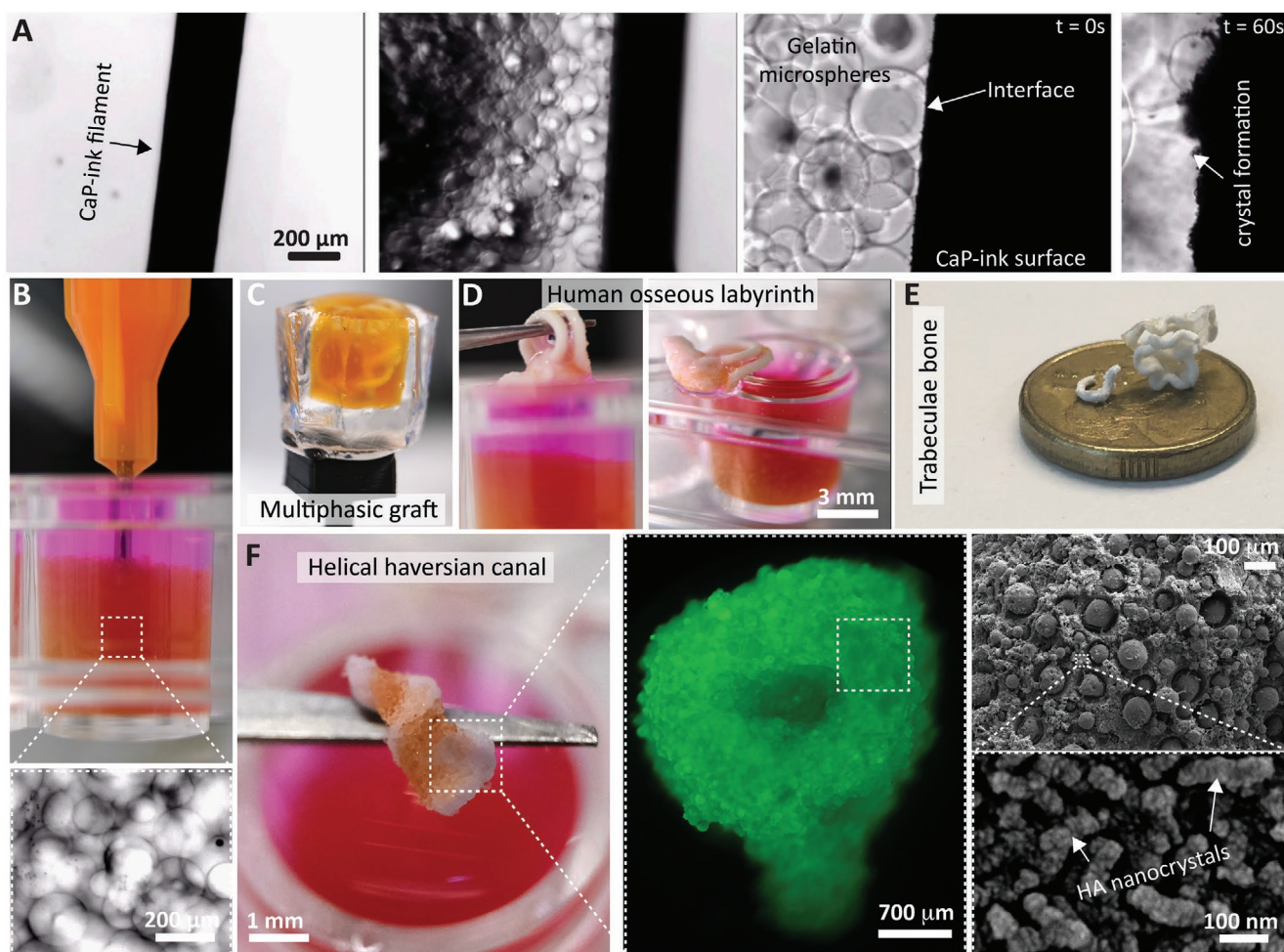


Figure 4. Generation of complex bone-mimetic architectures in a one-step procedure. A) Photographs of a printed CaP-ink filament within a gelatin microsphere support bath and interfacial adhesion during nanocrystal formation; B) front view of the printing process in a 96-well cell culture plate. Example of 3D constructs printed by COBICS: C) a heterogeneous biphasic structure mimicking osteochondral tissue using CaP-ink, gelatin microspheres and agarose hydrogel, and bone-like structures, such as D) human osseous labyrinth, E) trabecular bone, and F) helical Haversian canal. Magnification of printed BSA-FITC-labeled ink observed at epifluorescence microscope (F, middle) and at SEM to show formation of hydroxyapatite crystals postprinting (F, right).

the microspheres, and integration with tissue-specific cells will further expand the capabilities for mimicking complex tissue interfaces.

2.3. Ceramic Omnidirectional Bioprinting in Cell-Suspensions

Gelatin microspheres have been previously used for cell culture, either for preparation of viable cell aggregates^[35] or for controlling the fate of encapsulated stem cells.^[36] Therefore, we speculated that the addition of cells to the gelatin bath would facilitate adhesion and proliferation. For this purpose, we incorporated adipose-derived mesenchymal stem cells (ADSC) in the support bath, by mixing cells with cross-linked gelatin microspheres for 1 day, followed by printing with the CaP-ink. We tested cell concentrations of 5×10^3 and 1×10^4 cells mg^{-1} microspheres. Cell numbers were chosen based on previous studies of ADSC cultured in 3D matrices.^[36] All groups showed high cell viability when tested up to day 7, with higher cell

concentration corresponding to higher viability (Figure S5, Supporting Information). We then evaluated cell integration with the 3 different sizes of microspheres, S, M, and L, in the support bath. Across all groups, we observed no dead cells or any sign of toxicity (Figure S6A, Supporting Information). Cells cultured with the largest microspheres showed highest cell density, corresponding to 1500% viable cells after 14 days of culture and evidence for robust adhesion, spreading and proliferation (Figure S6B,C, Supporting Information). By increasing cell number from 1×10^4 to 5×10^4 cells mg^{-1} of microspheres in either S or M suspensions, both cell density and viability increased accordingly (Figure S6D,E, Supporting Information). Since printing fidelity decreases as microsphere size increases, we selected medium size suspensions for the remaining printing experiments.

Having established that cells could survive and proliferate within the microsphere suspension, we next explored biocompatibility of cells exposed directly to the CaP-ink. We used several types of cells that are associated with bone regeneration.

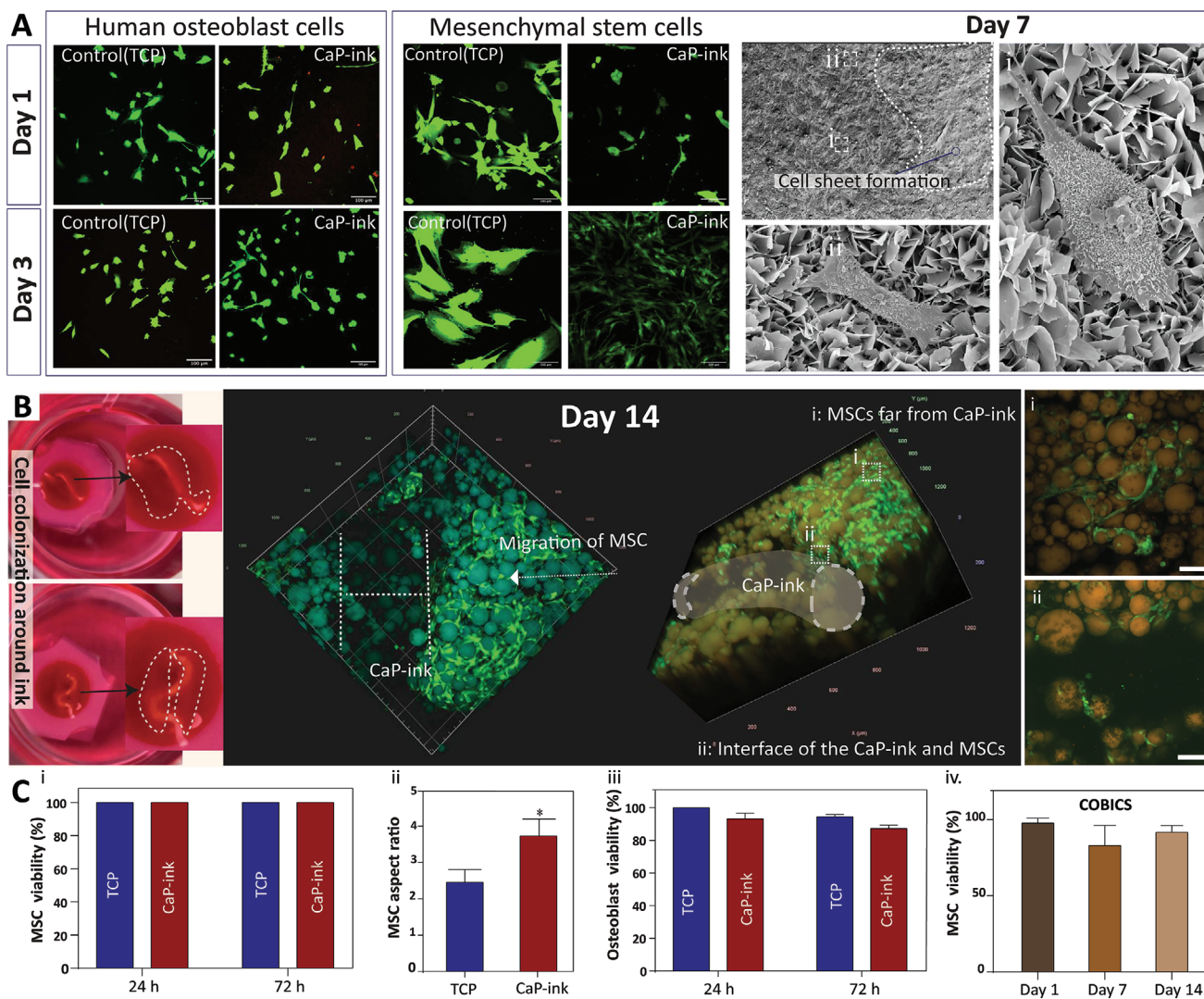


Figure 5. Cytocompatibility of bone-mimetic constructs. A) viability staining of mesenchymal stem cells (MSC), including bone-marrow MSC (BM-MSC) and adipose-derived MSC (ADSC), and osteoblast cells seeded on CaP-ink and scanning electron microscopy of MSC on CaP-ink after 7 days, showing the production of mineral nodules indicating the transition of MSC toward osteoblast. B) Top view of 3D printed construct after 7 days culture with mesenchymal stem cells (MSCs), showing tissue formation around the ink (left) and live-dead images of day 14 cell culture in COBICS (middle and right). C) Cell viability and cell shape analysis of MSC cultured on ceramic ink i,ii), cell viability of human osteoblasts on ink iii), MSC viability embedded within the support bath and migration of MSC toward CaP-ink iv).

We cultured mesenchymal stem cells (MSC), of either bone marrow (BM-MSC), or adipose tissue derivation (ADSC) (Figure 5A, middle), and bone-specific osteoblasts (Figure 5A, left) directly on rectangular-shaped scaffolds entirely composed of CaP-ink for up to 7 days. MSC adherent to the ceramic scaffold showed high viability (100%) after 24 and 72 h (Figure 5C, i).

Moreover, the MSC acquired an elongated shape, confirmed by cell aspect ratio quantification, when cultured for 3 days directly on the CaP-ink, compared to cells seeded on tissue culture plates (Figure 5C, ii). After 7 days of culture, MSC formed a dense cell sheet, with bone-like nodules arising from colony-forming units, which is suggestive of osteogenic differentiation, as shown previously using in vitro bone models with MSC³⁷ (Figure 5A, right, Figure S7, Supporting Information). Osteoblasts showed comparable viability to control on standard

tissue culture plates both at 24 h and 7 days (Figure 5C, iii). As an additional test of viability which relates indirectly to metabolic activity, Alamar blue assay was performed on the osteoblasts cultured on the same scaffolds (ink) after 24 and 72 h and compared to cells seeded on standard tissue culture plates (TCPS) and a commercially available hydroxyapatite scaffold (HA) (Figure S8, Supporting Information). Thus, we demonstrated the compatibility of the CaP-ink with cell types relevant to bone tissue engineering, such as MSC and osteoblasts.

Since cells showed compatibility with gelatin microspheres and CaP-ink individually, we next investigated the potential to fabricate a suspended free-form construct in the presence of living cells. A bath of gelatin microspheres was loaded with ADSC for printing 3D CaP-ink structures. Within hours we observed uniform cell integration within the support matrix.

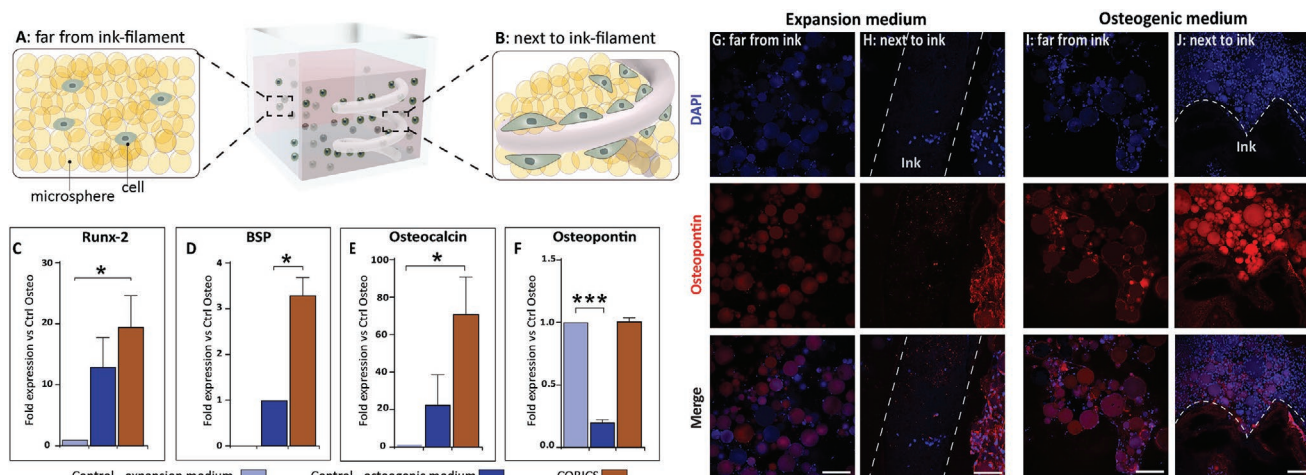


Figure 6. Differentiation of mesenchymal stem cells in 3D printed composites. Schematic representation of cells presents in gelatin bath, far from the ink A) and in proximity to the CaP-ink B). C–F) Osteogenic gene expression: Runx-2, bone sialoprotein (BSP), osteocalcin, and osteopontin, for cells cultured in COBICS composites in the absence of osteogenic supplements in culture medium, relative to tissue culture plates with and without osteogenic medium. Representative images of cells stained for osteopontin (red) in the vicinity of the CaP-ink H,I) and far from the CaP-ink G,I), either in expansion G,H) or osteogenic medium I,J). Nuclei were counterstained with DAPI (blue). Scale bars = 200 μ m.

After 14 days, cells appeared to proliferate within the gelatin matrix as well as along the gel-ink interface (Figure 5B; and Movie S6, Supporting Information) and were over 95% viable (Figure 5C, iv). On day 7, we noted a slight decrease in cell viability at the bone interface (Figure 4D, right), suggesting the onset of osteogenic differentiation as previously reported.^[38,39] Live/dead staining demonstrates high viability at day 1 ($97.71 \pm 3.24\%$), day 7 ($82.83 \pm 13.41\%$), and day 14 ($91.95 \pm 4.23\%$) (Figure 5D, iv).

2.4. Nanostructured Apatite Interfaces Promote Osteogenesis in Adipose-Derived Mesenchymal Stem Cells

To evaluate the osteogenic potential of COBICS structures, we performed gene and protein analysis of early, intermediate, and late-stage markers of osteogenesis in adipose-derived mesenchymal stem cells (ADSC) (Figure 6A,B). After 1 week of culture, reverse transcription-polymerase chain reaction (RT-PCR) analysis of cells transcripts when cultured in COBICS without osteogenic supplements, showed a 20-fold increase in the early marker Runx-2, compared to cells cultured on tissue culture plates and a twofold increase compared to cells cultured on tissue culture plates with osteogenic induction media (Figure 6C). Runx-2 is a master transcription factor associated with osteogenesis, as it has been shown to upregulate osteoblast-related genes, such as collagen type I, bone sialoprotein (BSP), osteocalcin, and alkaline phosphatase.^[40] Furthermore, markers for later phases of osteogenesis, including BSP (Figure 6D), osteocalcin (Figure 6E), and osteopontin (Figure 6F)^[41] were similarly up-regulated compared to cells cultured on standard plates. Remarkably, cells cultured on COBICS showed a further increase in expression compared to cells cultured in the presence of biochemical factors commonly used for inducing in vitro osteogenic differentiation. Other ceramic biomaterials, such as HA scaffolds, have shown

two- to threefold increased expression of early markers (Runx-2).^[42] However, only osteocalcin showed a similar increase compared to COBICS.^[43] Osteopontin is a bone extracellular matrix protein, known to peak twice in its expression: around day 4, during proliferation, and between days 14 and 21, during mineralization.^[44,45] Cells in COBICS showed gene expression comparable to control cells in proliferation medium and increased expression compared to control cells in differentiation medium, suggesting a slower differentiation rate than control cells chemically stimulated to differentiate into osteoblasts (Figure 6F; and Figure S9, Supporting Information). All together, these results suggest that our CaP-ink itself is a highly osteoinductive material.

Osteopontin expression was confirmed by protein analysis, both in expansion media (Figure 6G,H) and when supplemented with osteogenic factors (Figure 6I,J). Under growth conditions, cells expressed osteopontin only in close proximity to the CaP-ink and when adherent to the ink itself (Figure 6H), whereas cells far from the ink did not show positive expression (Figure 6G). When cultured in osteogenic media cells express osteopontin throughout the multiphasic construct (Figure 6I,J). In conclusion, we demonstrated that ADSC lineage specification was influenced directly by the CaP-ink, where close contact with the printed structure enhanced osteogenesis.

3. Conclusion

In this study, a new 3D printing technique, COBICS, was developed. This approach enabled unprecedented generation of mineralized constructs in a support bath containing live cells and microgels, mimicking the complex and hierarchical structure of native bone. The cells showed robust adhesion and proliferation behavior during printing, with greater than 95% viability after several weeks in culture. Lineage specification was dictated by proximity to the bone-mimicked constructs, where

close contact with the printed structure enhanced osteogenesis. The tendency for cells to differentiate at the interface of the constructs, while remaining multipotent in the intervening spaces, opens the potential for fabricating gradient tissue structures and intervening vasculature. Ultimately, this approach enables the in situ fabrication of bone-like tissues with the potential for use in bone tissue engineering applications, disease modeling, and drug screening.

4. Experimental Section

Ceramic Ink Fabrication and Characterization: Glycerol (C₃H₈O₃, product number: G9012), polyoxyethylenesorbitan monooleate (C₃₂H₆₀O₁₀, P6224), ammonium phosphate dibasic (NaHPO₄, A5764), calcium hydrogen phosphate (CaHPO₄, C7263), and calcium carbonate (CaCO₃, 310034) were all purchased from Sigma-Aldrich. α -TCP powder was synthesized by mixing calcium carbonate and calcium hydrogen phosphate in a zirconia crucible at a 1:2 m ratio. The crucible was placed into a high-temperature elevator furnace and the temperature increased to 1400 °C at a heating rate of 5 °C min⁻¹ and holding time of 5 h. At 1400 °C, samples were quickly removed from the furnace and quenched to room temperature. The obtained agglomerates were manually crushed by a mortar and pestle to achieve coarse powder with of particle size of less than 200 μ m using stainless steel sieves. The α -TCP powder was further ground using a planetary ball mill equipped with zirconia jars and grinding balls in ethanol (weight ratio of ball: powder = 8, ethanol: powder = 3, size of zirconia balls = 3 mm (2 h, at 180 rpm) and 1 mm (2 h, at 180 rpm) to obtain fine α -TCP powder with a narrow size distribution (D10 = 1.34 μ m, D50 = 2.86 μ m, and D90 = 6.19 μ m). To fabricate the ink, at the first stage the oil phase, surfactant and accelerator salt were mixed together. In a typical procedure, 5 wt% NaHPO₄, 28 wt% glycerol, and 6.5 wt% polyoxyethylenesorbitan monooleate were mixed in a zirconia jar for 5 min at 200 rpm. In the second stage, α -TCP powder (60.5 wt%) was added to the jars and homogenized with the suspension of precursors for 30 min to form a paste. Using a spatula, the paste was mixed manually and then homogenized further using the planetary ball mill for 30 min. At this point, paste either transferred to a syringe for printing or kept in a freezer (-20 °C). Scanning electron microscopy (FEI Nova NanoSEM 450 FE-SEM) and X-ray diffraction technique (The PANalytical Xpert Multipurpose X-ray diffraction system) was used to study the microstructure and chemistry of the ink after the setting. The kinetics of the setting reaction and the associated time-dependent changes in viscous and elastic behavior were characterized using an Anton Paar MCR 302 rotational rheometer with a 25 mm stainless steel parallel plate configuration. The ink was transferred between the plates under the dry and humid condition at 37 °C and then subjected to time-dependent oscillatory shear at a frequency of 1 rad s⁻¹ and a strain amplitude of 0.04.

Ink was characterized by the following properties: injectability, cohesion, printability, and setting time (Figure S2H, Supporting Information). Injectability was defined as the full extrusion of ink from a 1 mL Terumo syringe equipped with a stainless-steel tip (with an internal diameter of 600 μ m). The printability was defined as the dimensional integrity of ink filaments after extrusion from a nozzle. Cohesion was defined as the physical stability of ink filaments extruded into PBS (pH 7.4) using nozzles with diameter of 220, 600 μ m, and 1 mm. The setting time was defined as the duration after injection when extruded filaments in PBS with 1 mm in diameter do not deform being pushed by a spatula and the whole filament translocates alongside the spatula travelling direction.

For ceramic ink disks, cuboid shaped scaffolds were prepared by filling molds of 10 mm (length) \times 10 mm (width) \times 3 mm (depth) with CaP-ink and let them set overnight at 37 °C and 5% CO₂, before using them to culture cells.

FITC-BSA Distribution: 2 g of ink was directly mixed with 100 μ L of FITC-BSA (100 μ g mL⁻¹) and then loaded into a 1 mL syringe. The syringe was loaded into the printer (Hyrel3D with a custom-designed extrusion printing head) and scaffolds were printed at room temperature into a petri-dish (8 \times 8 \times 2 mm³ in size with filament orientation = 90°). Sintered hydroxyapatite scaffolds were made by the robocasting technique and used as the control group. HA Scaffolds (5 \times 5 \times 5 mm³ in size with filament orientation = 90°) were washed with ethanol and dried at 120 °C for 2 days. Samples were then submerged into FITC-BSA solution (100 μ g mL⁻¹) for 3 h and washed several times with PBS. Both scaffold types had 600 mm strut size and their cross-sections were analyzed by epifluorescence microscope BX53F (Olympus).

Drug Release: Dexamethasone (D4902, Sigma-Aldrich) and ibuprofen (I4883, Sigma-Aldrich) were selected as the model drugs. The dexamethasone and ibuprofen were mixed in powder form with the ink to obtain scaffolds containing 1 mg of the drug. For the control group, sintered HA scaffolds were submerged into drug solution (1 mg mL⁻¹ in ethanol) for 3 h. Drug loaded scaffolds were washed with PBS several times and placed in airtight containers in PBS at 37 °C in a shaker incubator. At each time point, 3 mL of PBS removed to measure the amount of the released drug and 3 mL fresh PBS added to each container.

Computational Modeling: The gelatin microspheres were modeled in five different sizes, with diameter as 600, 500, 400, 300, and 200 μ m. Regarding geometrical variables of ink bar, two sizes (600 and 200 μ m in diameter), two geometrical shapes (straight and spiral shapes), and three spatial orientation, including vertical, 45° inclination and horizontal groups, were considered in this study. Figure 2B–D shows the two representative assemblies of the container, gelatin microspheres (600 and 300 μ m in diameter) and ink bar. The container and ink bar were the same in both conditions, and the ink bar was placed in the middle of the container. The gelatin microspheres were uniformly distributed in the rest of the container. More specifically, it can be found that the gelatin microspheres were staggeredly arranged layer by layer, in both vertical and centripetal directions, shown by the top view and transparent 3D view. The potential configuration of ink bars in the current study are as follows: straight bar with 600 μ m diameter, straight bar with 200 μ m diameter, and spiral bar with 200 μ m diameter, respectively. The spatial orientation of the ink bar for each group includes the horizontal, 45° inclined, and horizontal direction. Both mechanical and diffusional properties used in the present study are summarized in Table S1 (Supporting Information). It should be noticed that the oxygen diffusivity and solubility coefficient were measured at the specific working conditions when the surrounding temperature is 37 °C and the pressure is equal to the standard atmosphere pressure. All of the gelatin microspheres, ink bar and water were meshed by using linear tetrahedral elements. A sensitivity analysis of the finite element mesh was conducted to determine the appropriate elemental size. This step is used for avoiding the excessive computational cost and at the same time, ensuring the adequate accuracy of the simulation results. According to the results, the global mesh size was set as 30 μ m for all the assembled model. The gelatin microspheres with 600 μ m diameter was meshed with 440 696 linear tetrahedral elements (degree of freedom—DOF: 278 703), 500 μ m group was meshed with 598 606 linear tetrahedral elements (degree of freedom—DOF: 412 698), 400 μ m group was meshed with 775 780 linear tetrahedral elements (degree of freedom—DOF: 538 336), and 300 μ m group was meshed with 945 720 linear tetrahedral elements (degree of freedom—DOF: 629 685). The ink bar with 600 μ m diameter was meshed by 19 215 linear tetrahedral elements (degree of freedom—DOF: 118 59), and 200 μ m diameter group was meshed by 2215 linear tetrahedral elements (degree of freedom—DOF: 1467). In addition, the spiral ink bar was meshed by 37 244 linear tetrahedral elements (degree of freedom—DOF: 24 093). Dynamic/explicit module in Abaqus 2016 (ABAQUS, Inc, Providence, RI) was adopted to perform the finite element deformation analysis, as the simulation in this study is highly nonlinear, and includes the interaction between solids and fluids. The system was only under the load owing to gravity, and the gravitational acceleration (g) was set as 9.8 m s⁻². The boundary condition was applied on the bottom surface

of container, by kinematically constraining all the displacements. For the diffusion analysis, the Abaqus mass diffusion module was adopted. The surface concentration flux load was created to generate the gradient concentration of oxygen from the free surface (top surface) to the middle part of container and all the way to the bottom. The initial inlet concentration was set as 20 (% or mmol cm⁻³) and uniformly distributed around the top surface (Figure S3, Supporting Information).

Gelatin Microspheres Fabrication and Characterization: Gelatin type A (G2500 Sigma) was first dissolved in deionized water at 50 °C before sterile filtration. For size M particles and size L, an oil bath (Canola Oil) was prewarmed to 40 °C under slow and vigorous stirring respectively. A 2.66% v/v gelatin solution was added dropwise and allowed 10 min to stabilize in the emulsion. The bath was subsequently cooled down to 10 °C and held for 30 min before the addition of 20% v/v solution of 0.25% w/t glutaraldehyde in acetone (Sigma). The particles were allowed 4 h to dehydrate and crosslink before decanting the mixture into centrifuge tubes to be extensively washed with acetone. The microparticles were then sonicated for 30 s before being stored in an acetone solution until further use. For the size S particles, 1.5% w/t of span 80 (Sigma) was added to the oil bath prior to the addition of gelatin to stabilize the emulsion. The bath temperature was also prewarmed to 55 °C at the start. For the control samples, 4 h of mixing with the glutaraldehyde-acetone solution was replaced with 1 h of mixing with pure acetone.

Cell Culture: Human osteoblasts (hOF) and human bone marrow derived stem cells (BM-MSC) were used to test ink biocompatibility. hOF were purchased from American Type Culture Collection (ATCC) and cultured in a 1:1 mixture of Ham's F12 medium Dulbecco's modified Eagle's medium, with 2.5 × 10⁻³ M L-glutamine (Gibco) supplemented with 10% fetal bovine serum (Bovogen) and 1% penicillin/streptomycin (Invitrogen), to which hereon as osteoblast media will be referred. BM-MSC were acquired by Lonza, cultured and expanded in fully supplemented mesenchymal stem cell basal medium (Lonza) according to the manufacturer's instructions. Human ADSC were obtained from ATCC, cultured and expanded in fully supplemented Mesenchymal Stem Cell Basal Medium for Adipose, Umbilical and Bone Marrow derived MSC (ATCC). All cells were then cryopreserved in 10% dimethyl sulfoxide solution at passage 2. Both BM-MSC and ADSC were subsequently thawed and cultured in the so-called complete medium, containing Dulbecco's modified Eagle's medium and low glucose (1000 mg L⁻¹) (DMEM, Invitrogen) media supplemented with 10% fetal bovine serum (Bovogen) and 1% penicillin/streptomycin (Invitrogen). hOF were thawed and cultured in the osteoblast media.

Medium was changed every 3 days, and cells were passaged at 70% confluency using a solution containing 0.25% trypsin/1 × 10⁻³ M. Cells were then used for experiments between passage 4 and 9. When requested, ADSC were switched to osteogenic culture media, consisting of DMEM supplemented with 100 × 10⁻⁹ M dexamethasone, 10 × 10⁻³ M β-glycerol phosphate, and 0.05 × 10⁻³ M ascorbic acid (all from Sigma-Aldrich).

COBICS Printing Process: The printer used in this study is a multihead printer (Engine HR, Hyrel 3D, USA) equipped with a customized extruder (EMO-25) for COBICS. For CaP-ink extrusion, 1 mL of ink was loaded into a 3 mL printing syringe and syringe was inserted in the EMO-25 extruder. All needles used in the study were purchased from Nordson EFD with inner diameter of 0.2–0.8 mm. The compressive strength of scaffolds was measured using uniaxial compressive tests utilizing a universal testing machine equipped with a 5 kN load cell at a constant crosshead speed of 1 mm min⁻¹. Five specimens for each porosity (≈85%, 70%, 60%, 50%, 40%, and 30%) was tested. The target porosity was obtained by varying spacing between the filaments (changing the pore size). The compressive strength was calculated by dividing the maximum load at the fracture point by the cross-sectional area of the samples. The scaffolds with strut size of 0.8 mm and orientation of filaments of 0°/90° were printed at room temperature using a Gcode to obtain scaffolds with 8 × 8 × 8 mm³ in dimension. The scaffolds were tested 7 days after incubation in PBS at 37 °C. For printing bone mimicked structures, the computer model was created by Autodesk

Fusion 360 and then converted to STL file (Figure S4, Supporting Information) prior to generating the Gcode. A 0.2 mm needle was used to print the constructs in 96 wells of cell culture plates containing gelatin microspheres and culture medium. After printing, constructs were kept in supporting bath for 6 min in order for the setting reaction to complete then they were removed by tweezers.

For the development of COBICS construct including cells, 2% agarose cylindrical shape well molds (5 × 3 mm) (Sigma-Aldrich) were used to contain the COBICS construct. One day before printing, 6 × 10⁵ ADSC were mixed with 12 mg gelatin microspheres and deposited in each agarose mold containing complete media. On the following day, CaP-ink was extruded in the gelatin-cell bath with a 1 mL syringe and 23 gauge tips (Nordson) and incubated at 37 °C and 5% CO₂. Samples were kept up to 14 days and media was changed every second day.

Rheological Analysis of Gelatin Microspheres Bath: All rheological measurements were performed on an Anton Paar MCR 302 Rheometer with parallel plate geometry (25 mm disk, 1 mm measuring distance) at 25 °C. The gelatin microsphere bath was prepared the same way as for printing experiments, and 600 μL of bath was added to the instrument stage. Oscillatory measurements were taken with a 1 Hz frequency with a log ramp of shear strain rate from 0.05 to 100% s⁻¹ over the course of 10 min.

Live Dead Assay: Live/dead assay was performed to both assess viability of cells directly cultured on ink-based disks and when cells were cultured in the COBICS system. For this purpose, cell viability was analyzed up to 14 days culture. To briefly describe the protocol used, cultured media was removed from each sample, which was then washed with Dulbecco's phosphate-buffered saline (DPBS, Gibco). After removing DPBS, samples were incubated with a solution of DPBS containing 2 × 10⁻³ M calcein (Thermo Fisher Scientific) and 4 × 10⁻³ M ethidium homodimer-1 (Thermo Fisher Scientific) at 37 °C for 1 h. Following, staining solution was removed, samples were washed with DPBS and transferred in a glass bottom dish for imaging through Nikon A1 confocal microscope at 488 nm to detect live cells and 543 nm for dead cells. Cell viability was then quantified using Image-J software.

Cell Fixing, Staining, and Confocal Imaging: Cells were fixed in 4% paraformaldehyde (Sigma-Aldrich) at 4 °C for 24 h. Samples were then treated with a protocol for clearing, which included a first step of 2 days incubation at RT in a solution for decolorization and delipidation containing (25 wt% urea, 25 wt% N,N,N',N'-tetrakis(2-hydroxypropyl) ethylenediamine and 15 wt% Triton X-100 (all Sigma). Following, after several PBS washings, samples were incubated with primary antibodies against the osteogenic markers, antiosteocalcin (1:100, Sigma-Aldrich) and antiosteopontin (1:100, Abcam) at RT for 1 day, and then with secondary antibodies antimouse Alexa Fluor 488 (1:200; Thermo Fisher Scientific), antirabbit Alexa Fluor 647 (1:200, Thermo Fisher Scientific) and DAPI (Sigma-Aldrich). Samples were then incubated in CUBIC-2, containing a mixture of 50 wt% sucrose, 25 wt% urea and 10 wt% 2,2'-nitrotriethanol (all Sigma) for another 2 days at RT, and then imaged immersed in same solution for matching the refractive index, by Nikon A1 confocal microscope. Images were collected using the following laser wavelength settings: DAPI using 405 nm, osteocalcin using 488 nm, and osteopontin using 645 nm.

Quantitative RT-PCR Analysis: For mRNA expression analysis of ADSC cultured either in standard TCP or in COBICS system, cells were maintained in culture for the required days at 37 °C, in 5% CO₂ and 20% O₂. Subsequently, cells were collected from each sample by trypsin treatment, and standard RNA isolation protocol was performed according to the manufacturer's instructions (Qiagen). Five hundred nanograms of total RNA was reverse transcribed into cDNA with a random hexamer primer using high-capacity cDNA reverse transcription kit (Applied Biosystems) according to the manufacturer's instructions and then RT-PCR was performed using CFX96 real-time detection system (Biorad). The reaction mixture was composed of 10 μL of SYBR Select Master Mix (Applied Biosystems), 10 pmol each of the forward and reverse primers, 2 μL of cDNA, and distilled water to a final volume of 20 μL. The thermocycling conditions were 95 °C for 30 s, followed by 40 cycles of 95 °C for 5 s and 60 °C for 34 s. Normalization of the

data was performed using the housekeeping gene glyceraldehyde-3-phosphate dehydrogenase (GAPDH) as an endogenous control in the same reaction as the gene of interest. The primers used in this study are listed in Table S2 (Supporting Information). The specificity of the SYBR PCR signal was confirmed by melt curve analysis. Ct values were transformed into relative quantification data using the $2^{-\Delta\Delta C_t}$ method, and data were normalized to GAPDH mRNA expression.

Statistical Analysis: Statistical analyses were performed using GraphPad Prism (version 8) software with 3–5 samples analyzed for each experimental group. One-way analysis of variance (ANOVA) was used for analysis of variance to compare between groups. Results are provided as mean \pm standard deviation of $n \geq 3$ independent experiments. Values were considered significant when $p < 0.05$.

Supporting Information

Supporting Information is available from the Wiley Online Library or from the author.

Acknowledgements

The authors would like to acknowledge the Biomedical Imaging Facility (BMIF) and the Electron Microscopy Unit at UNSW for providing assistance in using instruments for imaging component of this study. They also would like to thank Adam Feinberg at Carnegie Mellon University for assistance with building the 3D printers. The authors would like to acknowledge the National Health and Medical Research Council (Grant Nos. GNT1111694 and GNT1141602) and the Australian Research Council (No. FT180100417, FL150100060 and CE14100036).

Conflict of Interest

The authors declare no conflict of interest.

Data Availability Statement

Data sharing is not applicable to this article as no new data were created or analyzed in this study.

Keywords

3D printing, bone, ceramic, hydrogels, tissue engineering

Received: September 26, 2020

Revised: December 14, 2020

Published online:

- [1] Y. V. Shih, S. Varghese, *Biomaterials* **2019**, *198*, 107.
- [2] L. Wang, L.-X. Zhu, Z. Wang, A.-J. Lou, Y.-X. Yang, Y. Guo, S. Liu, C. Zhang, Z. Zhang, H.-S. Hu, B. Yang, P. Zhang, H.-W. Ouyang, Z.-Y. Zhang, *Biomaterials* **2018**, *175*, 44.
- [3] J. Chen, L. Deng, C. Porter, G. Alexander, D. Patel, J. Vines, X. Zhang, D. Chasteen-Boyd, H.-J. Sung, Y.-P. Li, A. Javed, S. Gilbert, K. Cheon, H.-W. Jun, *Sci. Rep.* **2018**, *8*, 15749.
- [4] M. R. Nelson, K. Roy, *J. Mater. Chem. B* **2016**, *4*, 3490.
- [5] N. Annabi, A. Tamayol, J. A. Uquillas, M. Akbari, L. E. Bertassoni, C. Cha, G. Camci-Unal, M. R. Dokmeci, N. A. Peppas, A. Khademhosseini, *Adv. Mater.* **2014**, *26*, 85.
- [6] M. Hippler, E. D. Lemma, S. Bertels, E. Blasco, C. Barner-Kowollik, M. Wegener, M. Bastmeyer, *Adv. Mater.* **2019**, *31*, 808110.
- [7] N. Reznikov, J. A. M. Steele, P. Fratzl, M. M. Stevens, *Nat. Rev. Mater.* **2016**, *1*, 16041.
- [8] S.-I. Roohani-Esfahani, P. Newman, H. Zreiqat, *Sci. Rep.* **2016**, *6*, 19468.
- [9] K. Lin, R. Sheikh, S. Romanazzo, I. Roohani, *Materials* **2019**, *12*, 2660.
- [10] M. Zhang, R. Lin, X. Wang, J. Xue, C. Deng, C. Feng, H. Zhuang, J. Ma, C. Qin, L. Wan, J. Chang, C. Wu, *Sci. Adv.* **2020**, *6*, eaaz6725.
- [11] J. W. Kim, B. E. Yang, S. J. Hong, H. G. Choi, S. J. Byeon, H. K. Lim, S. M. Chung, J. H. Lee, S. H. Byun, *Int. J. Mol. Sci.* **2020**, *21*, 1.
- [12] A. Lode, K. Meissner, Y. Luo, F. Sonntag, S. Glorius, B. Nies, C. Vater, F. Despang, T. Hanke, M. Gelinsky, *J. Tissue Eng. Regen. Med.* **2014**, *8*, 682.
- [13] G. Thirivikraman, A. Athirasala, R. Gordon, L. Zhang, R. Bergan, D. R. Keene, J. M. Jones, H. Xie, Z. Chen, J. Tao, B. Wingender, L. Gower, J. L. Ferracane, L. E. Bertassoni, *Nat. Commun.* **2019**, *10*, 3520.
- [14] P. N. Bernal, P. Delrot, D. Loterie, Y. Li, J. Malda, C. Moser, R. Levato, *Adv. Mater.* **2019**, *31*, 1904209.
- [15] A. E. Jakus, A. L. Rutz, S. W. Jordan, A. Kannan, S. M. Mitchell, C. Yun, K. D. Koube, S. C. Yoo, H. E. Whiteley, C. P. Richter, R. D. Galiano, W. K. Hsu, S. R. Stock, E. L. Hsu, R. N. Shah, *Sci. Transl. Med.* **2016**, *8*, 358ra127.
- [16] I.-W. Chen, X.-H. Wang, *Nature* **2000**, *404*, 168.
- [17] K. Zhang, Y. Fan, N. Dunne, X. Li, *Regen. Biomater.* **2018**, *5*, 115.
- [18] H. Lapczynska, L. Galea, S. Wüst, M. Bohner, S. Jerban, A. Sweedy, N. Doebelin, N. van Garderen, S. Hofmann, G. Baroud, R. Müller, B. von Rechenberg, *Eur. Cell. Mater.* **2014**, *28*, 299.
- [19] A. Kumar, S. Mandal, S. Barui, R. Vasireddi, U. Gbureck, M. Gelinsky, B. Basu, *Mater. Sci. Eng., R* **2016**, *103*, 1.
- [20] C. Wang, W. Huang, Y. Zhou, L. He, Z. He, Z. Chen, X. He, S. Tian, J. Liao, B. Lu, Y. Wei, M. Wang, *Bioact. Mater.* **2020**, *5*, 82.
- [21] T. Ahlfeld, F. Doberenz, D. Kilian, C. Vater, P. Korn, G. Lauer, A. Lode, M. Gelinsky, *Biofabrication* **2018**, *10*, 045002.
- [22] P. Diloksumpan, M. ne De Ruijter, M. Castilho, U. Gbureck, T. Vermonden, P. R. Van Weeren, J. Malda, R. Levato, *Biofabrication* **2020**, *12*, 025014.
- [23] J. Yang, Y. S. Zhang, K. Yue, A. Khademhosseini, *Acta Biomater.* **2017**, *57*, 1.
- [24] S. Yue, H. He, B. Li, T. Hou, *Nanomaterials* **2020**, *10*, 1511.
- [25] E. Gentleman, R. J. Swain, N. D. Evans, S. Boonrungsiman, G. Jell, M. D. Ball, T. A. V. Shean, M. L. Oyen, A. Porter, M. M. Stevens, *Nat. Mater.* **2009**, *8*, 763.
- [26] Y. Zhao, Z. Li, Y. Jiang, H. Liu, Y. Feng, Z. Wang, H. Liu, J. Wang, B. Yang, Q. Lin, *Acta Biomater.* **2020**, *113*, 614.
- [27] J. D. Kretlow, A. G. Mikos, *Tissue Eng.* **2007**, *13*, 927.
- [28] M. P. Ginebra, C. Canal, M. Espanol, D. Pastorino, E. B. Montufar, *Adv. Drug Delivery Rev.* **2012**, *64*, 1090.
- [29] T. Bhattacharjee, S. M. Zehnder, K. G. Rowe, S. Jain, R. M. Nixon, W. G. Sawyer, T. E. Angelini, *Sci. Adv.* **2015**, *1*, 4.
- [30] T. J. Hinton, Q. Jallerat, R. N. Palchesko, J. H. Park, M. S. Grodzicki, H.-J. Shue, M. H. Ramadan, A. R. Hudson, A. W. Feinberg, *Sci. Adv.* **2015**, *1*, e1500758.
- [31] A. Lee, A. R. Hudson, D. J. Shiwardski, J. W. Tashman, T. J. Hinton, S. Yerneni, J. M. Bliley, P. G. Campbell, A. W. Feinberg, *Science* **2019**, *365*, 482.
- [32] O. Jeon, Y. Bin Lee, H. Jeong, S. J. Lee, D. Wells, E. Alsberg, *Mater. Horiz.* **2019**, *6*, 1625.
- [33] N. Noor, A. Shapira, R. Edri, I. Gal, L. Wertheim, T. Dvir, *Adv. Sci.* **2019**, *6*, 1900344.
- [34] H. Babin, E. Dickinson, *Food Hydrocolloids* **2001**, *15*, 271.
- [35] K. Hayashi, Y. Tabata, *Acta Biomater.* **2011**, *7*, 2797.

- [36] A. Kodali, T. C. Lim, D. T. Leong, Y. W. Tong, *Macromol. Biosci.* **2014**, *14*, 1458.
- [37] S. Mechiche Alami, S. C. Gangloff, D. Laurent-Maquin, Y. Wang, H. Kerdjoudj, *Stem Cells Transl. Med.* **2016**, *5*, 1587.
- [38] W. A. Müller, *Developmental Biology*, Springer, New York **1997**, pp. 222–227.
- [39] J. Grzesiak, A. Śmieszek, K. Marycz, *Cell Biosci.* **2017**, *7*, 2.
- [40] R. Florencio-Silva, G. R. D. S. Sasso, E. Sasso-Cerri, M. J. Simões, P. S. Cerri, *Biomed Res. Int.* **2015**, *2015*, 421746.
- [41] A. B. Shupp, A. D. Kolb, D. Mukhopadhyay, K. M. Bussard, *Cancers* **2018**, *10*, 182.
- [42] Z. Lu, S.-I. Roohani-Esfahani, G. Wang, H. Zreiqat, *Nanomed. Nanotechnol., Biol. Med.* **2012**, *8*, 507.
- [43] J. Zhou, C. Xu, G. Wu, X. Cao, L. Zhang, Z. Zhai, Z. Zheng, X. Chen, Y. Wang, *Acta Biomater.* **2011**, *7*, 3999.
- [44] B. Kulterer, G. Friedl, A. Jandrositz, F. Sanchez-Cabo, A. Prokesch, C. Paar, M. Scheideler, R. Windhager, K. H. Preisegger, Z. Trajanoski, *BMC Genomics* **2007**, *8*, 70.
- [45] J. E. Aubin, *Rev. Endocr. Metab. Disord.* **2001**, *2*, 81.